4.2. Slurry Bubble-Column Reactor (SBCR) Experiment

A slurry-bubble-column reactor (SBCR) experiment served as a test bed for diagnostics development and is shown in Figure 41. This test bed is capable of operation at the large pressures, temperatures, gas flow rates, and length scales of industrial interest. Despite its size, this bubble column enables implementation and modification of many, but not all, of the diagnostic techniques previously discussed. Optical techniques, such as flow visualization and LR, can be applied only in a limited sense through the view ports. Pressure-based techniques, such as DP, can be applied because of the availability of pressure ports through the side wall. Radiation-based techniques, such as GDT, can be used despite the thick, high-density side wall. The application of electrical techniques, such as BEI, EIT, and the EBP, inside the SBCR vessel remains a subject of research due to the conducting wall. Limited geometric modifications, such as installation of alternate spargers, probe rings, or internals, can be carried out without excessive difficulty.
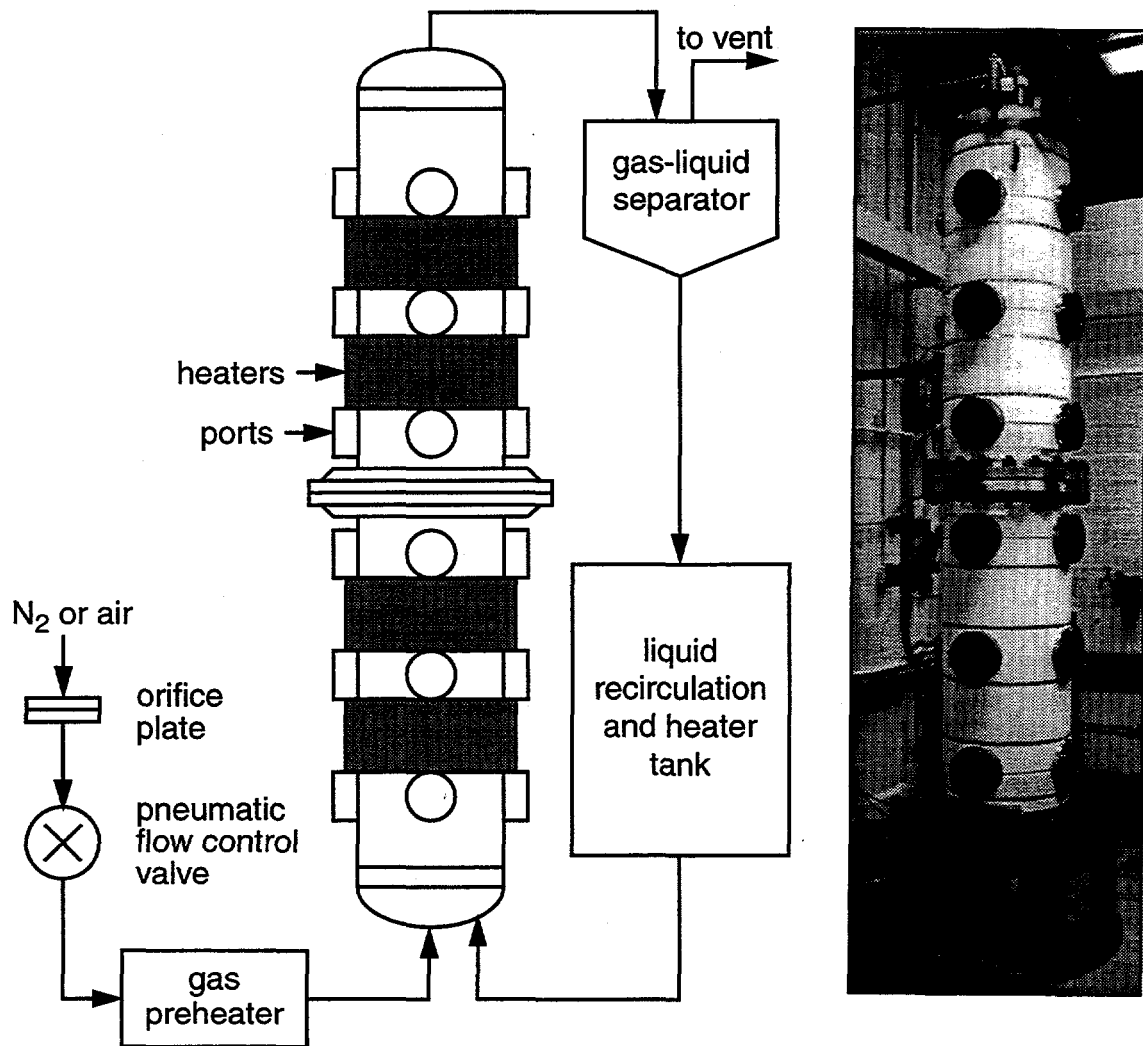

Figure 41. The slurry bubble-column reactor (SBCR) experiment.

4.2.1. SBCR Experimental Setup

An SBCR experiment, shown in Figure 41, has been utilized to facilitate development and validation of multiphase-flow diagnostics capable of operating at industrially relevant conditions. The vessel is made out of stainless steel and has an inner diameter of 0.48 m (19.0 inch), a height of 2.75 m, and a wall thickness of 1.27 cm (0.5 inch). The vessel has 12 visual ports and 12 instrumentation ports distributed at 6 vertical locations, with the 4 ports (2 of each type) at each vertical location separated by 90° intervals. Pressure transducers and thermocouples are installed at instrumentation ports at each vertical level and at other critical locations throughout the flow system. A computer-controlled data acquisition system and custom software are available to monitor, record, and control flow conditions.

The Sandia wind tunnel supply of clean, dry air is used to produce the air flow within the SBCR vessel. Gas is drawn from a 50 ft^3 surge tank, which is maintained at 255 psi by a 5200 ft^3 air storage tank. A sparger is used to introduce the gas into the vessel. The sparger is a 15 cm diameter toroidal ring formed from 1.1 cm diameter stainless steel tubing with 12 upward-facing holes with diameters of 0.3175 cm (0.125 inch) at equal azimuthal spacing. The gas velocity entering the vessel is set using a pneumatic flow control valve that uses the pressure drop across an orifice plate as the control parameter. Gas flow rates are calculated from the orifice plate pressure differential and other relevant flow conditions, and the pressure inside the vessel is maintained using a back-pressure regulator. Gas superficial velocities of up to 0.4 m/s, which produce churn-turbulent flows in most liquids, and gas volume fractions up to 0.4 can be routinely achieved in the SBCR vessel with this gas flow system. Gas is exhausted through a pipe with an inner diameter of 3.3 cm (1.3 inch) from the top of the vessel, passes through a cyclone gas-liquid separator to remove any entrained liquid droplets, and is vented to a fume hood duct leading to the roof.

Operation of the SBCR experiment is possible for pressures up to 690 kPa (100 psig) and for temperatures up to 200 °C. Elevated temperatures in the column are attained by preheating the gas to the desired temperature using a 50 kW preheater. Further temperature control is achieved by four sets of 3 kW silicone rubber heaters located at four axial locations along the vessel and covered by a layer of insulation. Each set of heaters is controlled separately, allowing the vessel to be maintained at either uniform or axially varying temperature distributions. Tests indicate that temperature uniformity can be maintained to within 2 K inside the vessel.

4.2.2. SBCR Experimental Results

Gas-liquid experiments have been performed in the SBCR vessel using water and Drakeol 10 with air sparging at several pressures (Adkins et al., 1996; Jackson et al., 1996ab). Drakeol 10 is a light mineral oil used in SBCRs. A wide pressure range was examined because gas-liquid bubble-column flow is known to depend significantly on pressure. The vessel is filled to four diameters above the sparger prior to initiating air flow, and GDT scans are taken two diameters above the sparger. Additionally, DP is used to determine average gas holdup values for the volumes between pairs of transducers. Figure 42 shows the DP gas holdup results for air-water and air-Drakeol 10 at gas superficial velocities up to 0.25 m/s and pressures up to 432 kPa (62.6 psia). Also shown are predictions of the Zuber-Findlay correlation (Zuber and Findlay, 1965):

$$\varepsilon_G = \frac{U_G}{C_0 U_G + C_1 [\zeta g (\rho_L - \rho_G)/\rho_L^2]^{1/4}} \approx \frac{U_G}{C_0 U_G + C_1 [\zeta g / \rho_L]^{1/4}}, \tag{57}$$

where ε_G is the average gas holdup, U_G is the gas superficial velocity, ρ_L and ρ_G are the liquid and gas densities, ζ is the surface tension, g is the gravitational acceleration, and both C_0 and C_1 are empirical coefficients determined from this data set so that the correlations fit this data set:

$$C_0 = \left\{ \begin{array}{l} 8.43\exp[-P/(138\ \text{kPa})]\ \text{air-water} \\ 3.83\exp[-P/(460\ \text{kPa})]\ \text{air-Drakeol 10} \end{array} \right\},\ C_1 = \left\{ \begin{array}{l} 1.53\ \text{air-water} \\ 2.13\ \text{air-Drakeol 10} \end{array} \right\}. \tag{58}$$

symbols: DP results
curves: Zuber-Findlay
with C_0, C_1 correlations

symbols: DP results
curves: Zuber-Findlay
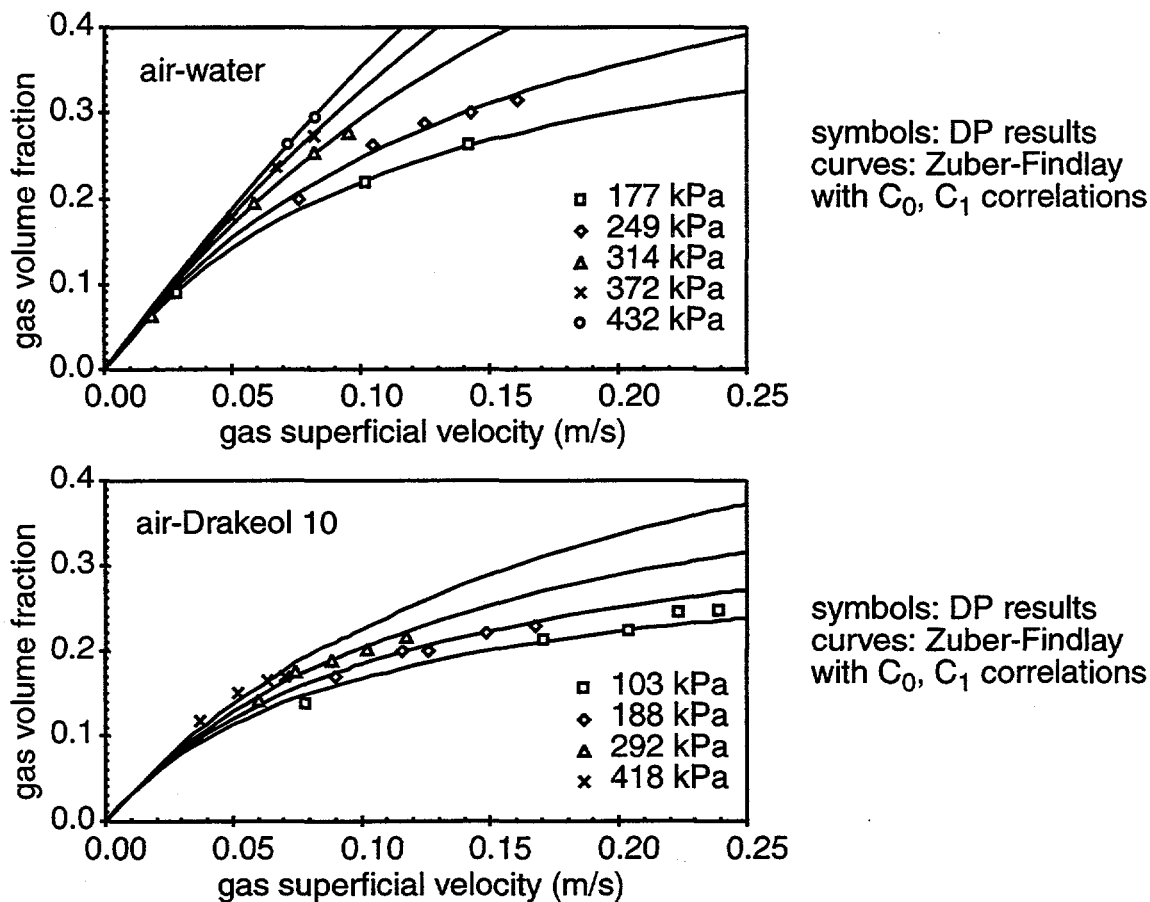with C_0, C_1 correlations

Figure 42. Gas volume fraction results from DP for gas-liquid flow in SBCR.

Figure 43 shows GDT results for gas-liquid experiments with air-water and air-Drakeol 10, with 30 s and 60 s of counting time per point, respectively. One GDT scan is shown for each liquid, and gas-volume-fraction radial profiles are shown as functions of gas superficial velocity and pressure. Gas volume fractions are significantly higher with water than with Drakeol 10 despite the fact that Drakeol 10 is 30 times as viscous as water. For both liquids, increasing the pressure while holding the gas superficial velocity constant increases the gas volume fraction uniformly throughout the flow, whereas increasing the gas superficial velocity while holding the pressure constant increases the gas volume fraction more near the axis than near the side wall.
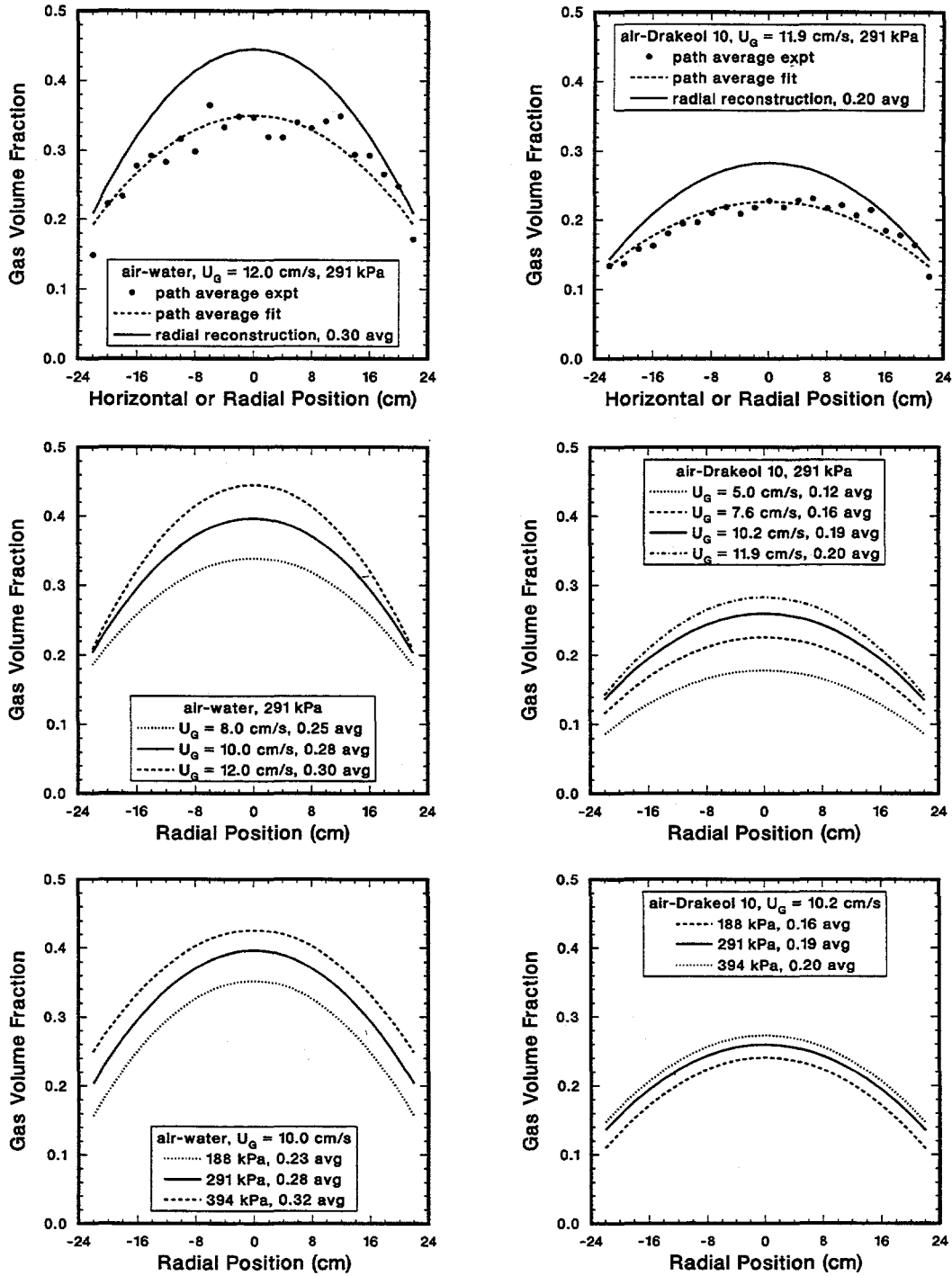
all scans at L/D = 2

Figure 43. Gas volume fraction results from GDT for gas-liquid flow in SBCR.

82

Table 4. Average gas volume fraction values from GDT and DP for air-water in SBCR.

P (kPa)	U_G (cm/s)	ε_G^{GDT}	ε_G^{DP}
141	12.5	0.21	0.21
208	14.6	0.27	0.25
253	15.7	0.29	0.29
230	8.6	0.20	0.20
285	10.8	0.25	0.25
330	12.0	0.28	0.31
299	6.6	0.19	0.20
360	8.6	0.24	0.24
390	10.2	0.27	0.29

Table 4 and Figure 44 show a comparison of the average gas volume fractions from GDT and DP for air-water and air-Drakeol 10 tests in the SBCR experiment. The DP results are plotted as a function of vertical position normalized by the SBCR vessel diameter and represent volumetric averages over approximately one diameter of height centered about the plotted points. The GDT results are shown as solid symbols. For a wide range of pressures and gas superficial velocities, the GDT and DP values are seen to be in reasonable agreement for the air-water tests. A similar comparison for air-Drakeol 10 does not yield quite as good agreement, with the GDT values slightly but systematically lower than the DP values. The cause of the discrepancy is not known at present and will be the focus of future investigations. It may be related to the fact that the gas volume fraction values determined by DP do not vary strongly with vertical position in the air-water tests, suggesting that the flow is nearly fully developed. For the air-Drakeol 10 tests, the DP results indicate that the gas distribution is changing considerably in the vertical direction. The DP technique is believed to be most accurate for fully developed flow, so the GDT results are conjectured to be more accurate for the air-Drakeol 10 tests. From these results it is clear that the range of applicability of DP continues to remain a topic of investigation.
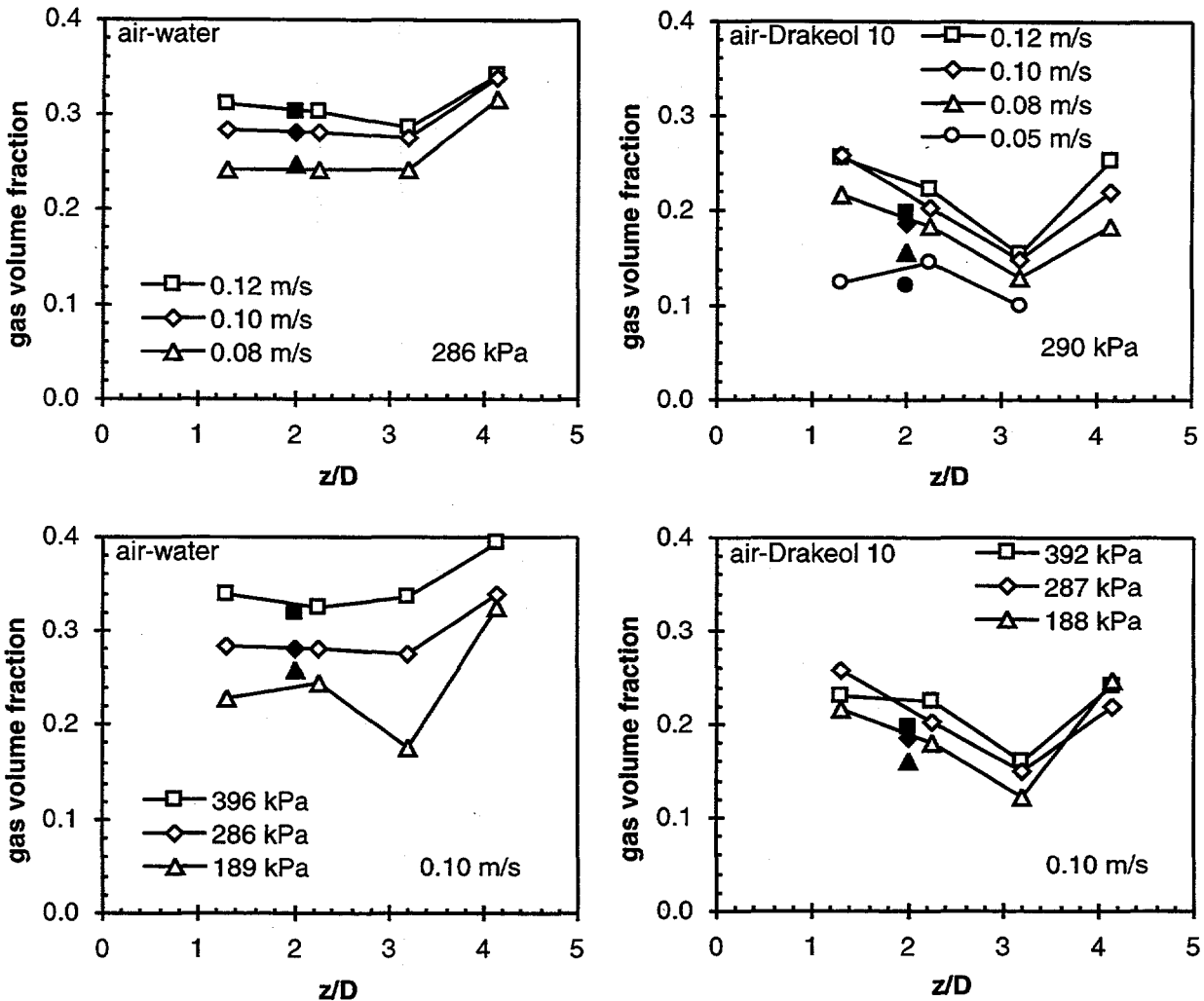
Figure 44. Gas volume fraction vertical variation from DP and GDT in SBCR.

4.3. Two-Phase Experiments Combining GDT and EIT

As has been previously discussed, measuring material distribution in three-phase flows requires application of two complementary diagnostic techniques, such as GDT and EIT. A necessary preliminary step en route to three-phase measurements is the application of GDT and EIT to two-phase flows since each technique should be capable of independently determining the phase volume fraction spatial variation. Since the GDT system has already been validated extensively for gas-liquid flows, as presented in previous sections, it can be used to assess the behavior the EIT system for multiphase-flow measurements. To this end, two types of multiphase flow are examined with both techniques: liquid-solid flows with dilute concentrations of small spherical insulating solid particles mixed uniformly in a conducting liquid, and gas-liquid flows in the TBC experiment. The latter is a more rigorous test since the gas bubbles are larger, nonspherical, deformable, densely concentrated, and nonuniformly distributed.

4.3.1. Liquid-Solid Flow (LSF) Experiment

A liquid-solid flow has been examined with both GDT and EIT to validate the quality of the measurements taken with EIT. A flow of particle-laden liquid was chosen for investigation for several reasons. First, the amount of solid introduced into the experiment can be carefully controlled and, for a closed volume, remains constant for all time. Knowledge of the average solid volume fraction thus provides a good check on the diagnostics. Second, unlike gas bubbles, solid particles can be small, uniform-diameter spheres that do not deform or otherwise change their shape during the experiment (so long as conditions are not harsh enough to fracture the particles). Third, a mixer can be employed to generate a relatively uniform distribution of solids throughout most of the flow geometry. Fourth, the solid particles and the liquid medium can be chosen without difficulty to have significantly different gamma attenuation coefficients and electrical conductivities so that both GDT and EIT can be applied to determine the phase volume fraction spatial variation.

Schematic diagrams of the experimental setup and diagnostics are shown in Figure 45. The flow apparatus consisted of a Lexan cylinder (19 cm inner diameter, 0.635 cm wall thickness, 76 cm height) closed at the bottom and the top, into which a mixer was inserted. A Sargent-Welch mixer (model S-76509-80B) was used. The mixer system consisted of a compact impeller assemblage positioned 1 cm above the bottom of the cylinder interior, a motor mounted above the top end of the cylinder, and a shaft (0.8 cm diameter with the coating, described below) connecting the impeller to the motor. The shaft passed through a small concentrically-positioned hole in the top end of the cylinder, around which an "overflow" volume was placed to ensure the absence of free-surface effects (e.g. a vortical "funnel" due to swirling) in the cylinder interior during mixing. A mixer speed of 600 rpm was used for all solid volume fractions, as needed to achieve a roughly uniform distribution (to the eye) of particles within the liquid. For solid volume fractions much in excess of 0.03, large fluctuating motions and solid volume fraction variations were visually apparent, so solid volume fractions were restricted in this study to no larger than about 0.03 although even at this value some solid volume fraction variations were discernible.

The nominal (volume-averaged) solid volume fraction $\varepsilon_s^{\text{NOM}}$ was specified in the following manner. Glass spheres with a mean diameter of 80 μm were used. A prescribed volume of these spheres, as determined by weight and the known density of the glass, was introduced into the cylinder, and water was added until the remaining volume was filled. Water was selected because its electrical conductivity can be adjusted by dissolving a small known amount of salt (sodium chloride) in it. Typical electrical conductivities of the salt-water solution were around 1 mS/cm. However, temperature variations and their effects on the precise ionic composition of water were large enough to alter the conductivity appreciably, necessitating the calibration measurements discussed below. Glass spheres were selected for the following reasons. First, they are fairly rugged and are easily separated from water by settling. Second, glass is an insulator compared to (non-deionized) water, so EIT can in principle discriminate between glass spheres and water. Third, glass attenuates gamma photons more strongly than does water, so GDT can also discriminate between glass and water.

The presence of the mixer shaft is somewhat problematic for both techniques. For GDT, it produces extra attenuation when the gamma beam passes through it. In this study, these anomalous points are not used in performing the reconstruction. For EIT, placing a good conductor like the mixer's steel shaft in the center of the cylinder would significantly distort the electric field lines, so the shaft and impeller were coated with a layer of insulating paint to mitigate this effect. The presence of a small-diameter (relative to the cylinder), concentrically-positioned, insulated inclusion was expected to have only a small effect on the electrical behavior of the system, and this was verified by taking EIT measurements using water (no particles) both with and without the mixer shaft.
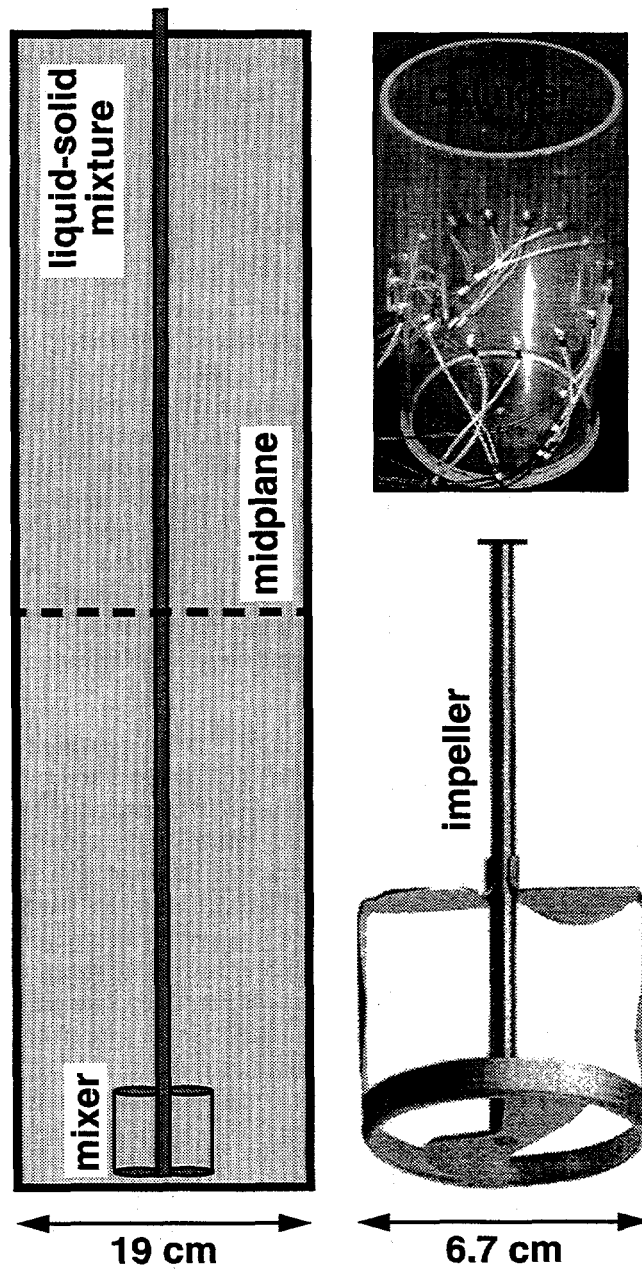
Figure 45. The liquid-solid flow (LSF) experiment.

Three sets of experiments were performed in this study, as summarized in Table 5. In each set, a prescribed amount of glass spheres was introduced to the cylinder, and the remainder of the volume was filled with water. Mixing was then initiated for a 30-minute period, which was determined to be long enough for the system to come to a statistically stationary state. GDT and EIT were successively applied, where the GDT and EIT scans required 4 and 10 minutes, respectively. Mixing was then terminated, and the solid-liquid mixture was allowed to remain quiescent for a 5-minute period, which was long enough for the spheres to settle to the bottom of the water-filled cylinder. Following this settling period, EIT was applied again. This second EIT measurement was necessary for calibration purposes because the conductivity of the water was altered by soluble contaminants unavoidably introduced when the spheres were added. Although this trace amount of contaminant material had a negligible effect on GDT, as verified by additional GDT measurements, its effect on the water conductivity was comparable in magnitude to that of the suspended solid particles.

Table 5. Conditions and results for LSF experiment.

| Case	ε_s^{NOM}	$[\mu_m/\mu_w]_{av}$	ε_s^{GDT}	$[\sigma_m/\sigma_w]_{av}$	ε_s^{EIT}
1	0.010	1.015	0.011	0.982	0.012
2	0.020	1.030	0.021	0.968	0.021
3	0.030	1.057	0.040	0.940	0.041

Figure 46 shows a compilation of results corresponding to the cases delineated in Table 5. One of the plots shows the GDT measurements of μ_m/μ_w, the path-averaged mixture attenuation coefficient normalized by the attenuation coefficient of water, as a function of x/R, the normalized horizontal position of the measurement path. The data points near $x = 0$ are anomalous because the gamma beam passes through or near the mixer shaft and are not shown. Several observations can be made from this plot. First, despite some variations due to the unsteady nature of the flow, the profiles are relatively uniform. Second, μ_m/μ_w increases monotonically with increasing ε_s^{NOM}. The GDT reconstruction algorithm was used for these cases to determine $[\mu_m/\mu_w]_{av}$, the average of μ_m/μ_w in the cross section, as shown in Table 5 and in Figure 46 plotted against ε_s^{NOM}. In these calculations, the attenuation coefficient profile was taken to be spatially uniform. Additional calculations performed using radially parabolic profiles were found to yield almost identical profiles and averages (the reconstructions were not improved significantly in quality by the additional degree of freedom). The $[\mu_m/\mu_w]_{av}$ values were converted into the solid volume fractions ε_s^{GDT} in Table 5 and in one of the plots in Figure 46 using the following relation:

$$\varepsilon_s^{GDT} = \frac{[\mu_m/\mu_w]_{av} - 1}{[\mu_s/\mu_w] - 1}, \tag{59}$$

where the attenuation coefficients of water and the glass spheres are given by $\mu_w = 0.0858$ cm^{-1} and $\mu_s = 0.209$ cm^{-1}. The EIT reconstruction code EITA3D was applied to determine $[\sigma_m/\sigma_w]_{av}$, the average electrical conductivity of the mixture normalized by that of the liquid, which is shown in Table 5 and in Figure 46 plotted against ε_s^{NOM}. Nearly identical average conductivities were obtained when using either a spatially uniform conductivity distribution or a radially parabolic distribution, so a uniform distribution was employed, being simpler and equally accurate for this experiment. The quantity $[\sigma_m/\sigma_w]_{av}$ is seen to decrease monotonically with increasing ε_s^{NOM}. The $[\sigma_m/\sigma_w]_{av}$ values were converted into the solid volume fractions ε_s^{EIT} in Table 5 with the Maxwell-Hewitt relation:

$$\varepsilon_s^{\text{EIT}} = \frac{1 - [\sigma_m/\sigma_w]_{\text{av}}}{1 + (1/2)[\sigma_m/\sigma_w]_{\text{av}}}. \tag{60}$$
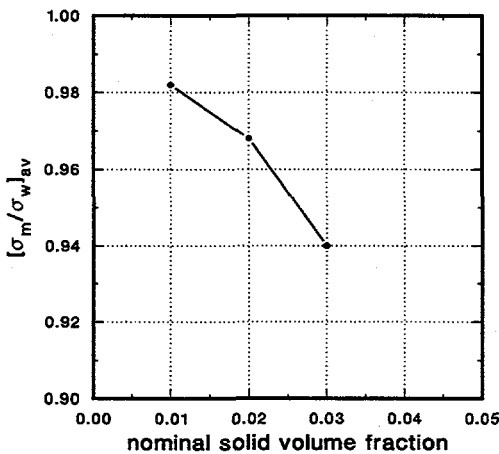
The solid volume fractions determined by GDT and EIT are in close agreement with each other for all cases and with the nominal values for the first two cases. Case 3 is interesting in that the GDT and EIT values are in agreement with each other but are somewhat higher than the nominal value. It is conjectured that the mixing may not have been strong enough to produce a uniform axial distribution of glass spheres throughout the cylinder for a nominal solid volume fraction of 0.03.
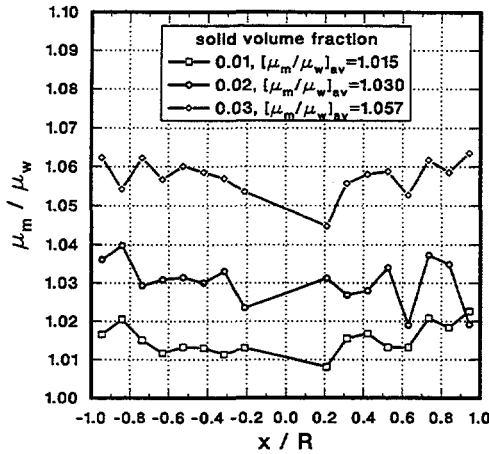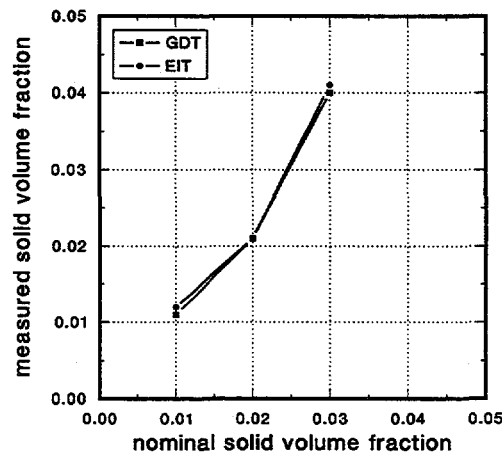

(a) GDT scans
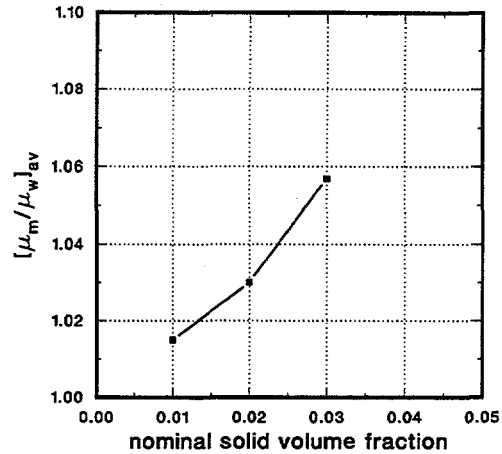
(b) average attenuation from GDT

(c) average conductivity from EIT

(d) volume fractions from GDT and EIT

Figure 46. Solid volume fraction results from GDT and EIT in LSF.

88

4.4. Application of GDT and EIT to TBC

As previously indicated, two types of information are required to determine material distribution in three-phase flows. For gas-liquid-solid flows, GDT and EIT are good candidates for such measurements. GDT is most sensitive to the presence of the dense phases (the liquid and the solid), EIT observes the presence of the conducting phases (usually the liquid), and the remainder of the volume is filled with the nondense nonconducting phases (usually the gas). However, EIT, being less technically mature than GDT, requires extensive validation in two-phase flows prior to application to three-phase flows, for which direct validation may not be possible. The LSF experiment was the first step toward this validation, employing a conducting liquid phase and an insulating solid phase. This experiment has several features not present in many two-phase flows of interest. The dispersed phase was composed of solid particles that were small compared to any macroscopic dimensions, approximately spherical, geometrically unchanging, volumetrically fairly dilute, and fairly uniformly distributed in space.

It is of interest to apply EIT to a two-phase system without these features as a more rigorous validation test. This is particularly important since the Maxwell-Hewitt relation relies on spherical particles that are small compared to the curvature of mean field lines and are randomly but statistically uniformly distributed in space. Bubble-column flows severely strain these assumptions at higher gas volume fractions. For example, a simple-cubic lattice of touching spheres has a volume fraction of $\pi/6 \approx 0.52$, so gas volume fractions around 0.4 (often observed) probably produce bubbles with shapes that are significantly deformed from spheres.

Two-phase gas-liquid flow in the TBC experiment was selected for this type of validation exercise. As in the LSF experiment, the dispersed phase (air bubbles) is insulating, and the liquid phase (water) is conducting. However, the bubbles are typically on the order of a few millimeters in diameter which is substantially bigger than the 80 μm glass spheres used in the LSF experiment and comparable to the electrode size in the EIT point-electrode probe ring. Bubbles of this size are fairly deformable, unlike the glass spheres, and gas volume fractions on the order of 0.3 can be routinely achieved, as opposed to the maximum value of about 0.04 encountered in the LSF experiment.

Both GDT and EIT were applied to the TBC experiment to measure material distribution in gas-liquid flow. Air and water were chosen to be the working fluids, and the toroidal-ring sparger was employed for these experiments. Figure 47 shows a schematic of the TBC experiment including the measurement plane (diagram at left), the TBC with the GDT system in place (photograph in middle), and the TBC with the EIT system in place (photograph at right). In this application, the EIT probe ring with point electrodes was employed. This probe ring samples the volume of the TBC experiment within plus or minus roughly one diameter of the measurement plane. As indicated previously for electrical techniques, a small amount of salt was added to the water to set the conductivity to approximately 1 mS/cm, and heaters placed at four vertical stations were active to prevent conductivity changes due to air-flow-induced evaporation of water.
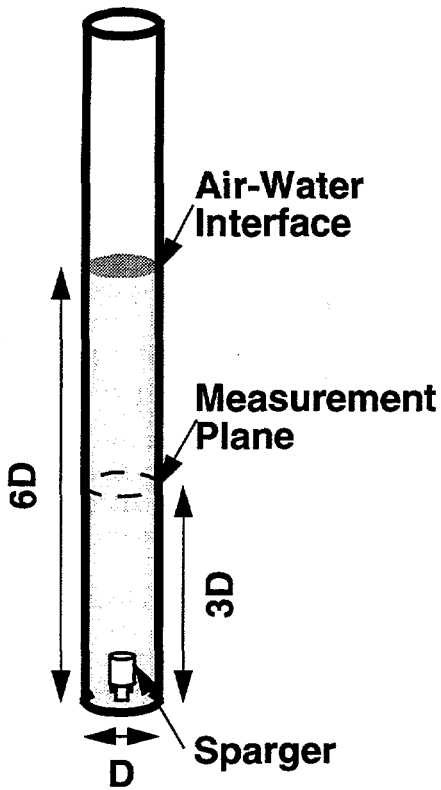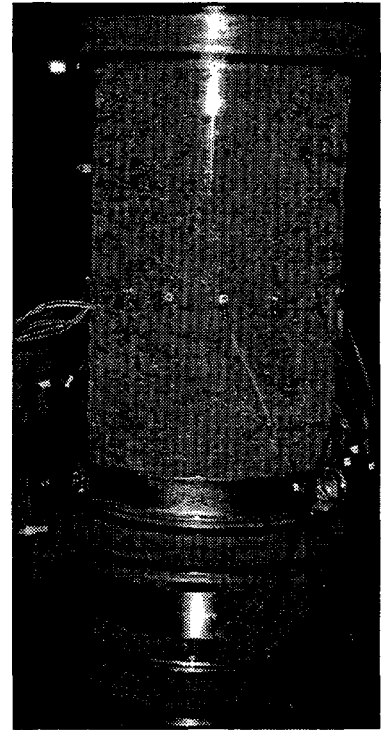
Figure 47. GDT and EIT installed in TBC for measuring gas-liquid flow.

Two air flow rates were examined in the TBC experiment: 100 and 200 lpm, which correspond to gas superficial velocities of 5.9 and 11.8 cm/s, respectively. GDT measurements were taken at 1 cm intervals across the measurement plane, and a parabolic attenuation profile was used to perform the reconstruction. Higher-degree polynomials were not found to give significantly different reconstructions. The EIT probe ring with 16 point electrodes was used to acquire voltage data, and the code EITA3D was used to perform the reconstructions. The EIT voltages used to perform the reconstructions were the averages of 6400 complete EIT measurements (i.e. each of the 1920 voltages from the 120 source-sink electrode pairs is measured 6400 times). A parabolic variation in conductivity was used by EITA3D to produce the reconstructions, and the Maxwell-Hewitt relation was used on a point-by-point basis to convert the conductivity profile into a gas volume fraction profile. Note that a parabolic conductivity profile is not transformed into a parabolic gas volume fraction profile by the Maxwell-Hewitt relation.
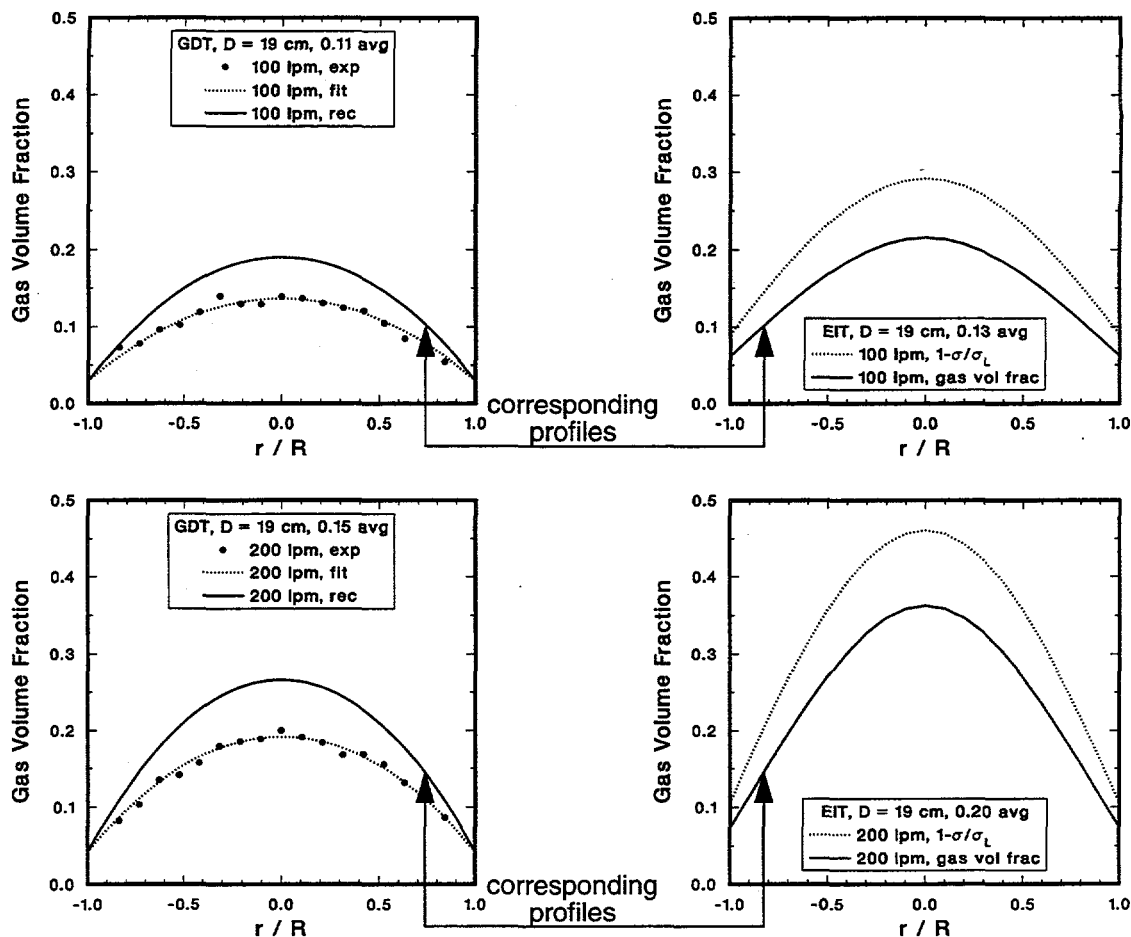
Figure 48. GDT and EIT results at same conditions in TBC.

Figure 48 shows GDT and EIT results in the TBC experiment for the two air flow rates examined. The GDT results are shown on the left, with symbols denoting the path-averaged values, the dotted curves denoting quadratic polynomials fits through the symbols, and the solid curves denoting the reconstructed gas volume fraction profiles. The GDT results exhibit high symmetry with the improved sparger design, suggesting that the assumption of axisymmetry is a good one although nonaxisymmetric variations cannot be rigorously ruled out. As is generally observed, the gas volume fraction is largest on axis and smallest at the side walls and increases preferentially near the axis with increasing gas flow rate. The EIT results are shown on the right side of Figure 48, with the dotted curves denoting the reconstructed conductivity profiles and the solid curves denoting the reconstructed gas volume fraction profiles. The EIT gas-volume-fraction profiles exhibit the same features but have somewhat higher values than the GDT profiles. The GDT profiles were found to be in good agreement with DP results and therefore are believed to be the more accurate. The over-prediction by EIT of the gas volume fraction in the TBC gas-liquid flows is reminiscent of the fact that EIT slightly but consistently overpredicted the diameters of ICIs: the amount of insulator is slightly overestimated in both types of validation exercises.

91

Several effects have been investigated or are currently under investigation as possible causes for this overprediction. The presence of a grounded conductor anywhere in the column was found to exert a profound effect on the EIT data, so all conducting fittings, including the sparger, were removed or electrically isolated prior to acquiring the data shown in Figure 48. Since the electrical conductivity of water decreases with decreasing temperature caused by evaporation, heaters were used to maintain a constant water temperature to within 0.1 K, which greatly reduces spurious changes in conductivity due to temperature. Other possibilities for the observed discrepancy include electronics and capacitive effects, electrode size (comparable to bubble size so that bubbles could conceivably cover electrodes), the parabolic representation of the conductivity spatial variation in the code EITA3D, the Maxwell-Hewitt relation used to convert electrical conductivity to gas volume fraction, and temporal averaging that occurs due to the time needed to acquire a data set.

The most likely causes of the discrepancy probably are capacitive effects, electrode size, temporal averaging, and the parabolic representation of the conductivity field. These will be systematically addressed in the next EIT probe ring, which is currently under development. Electrodes will be somewhat larger, perhaps about 1 cm in diameter, and only 8 electrodes will be used. This will increase the signal-to-noise ratio by considerably reducing the voltage drop experienced when current enters or exits the multiphase flow so that the voltage differences between electrodes will be a much larger proportion of the total voltage difference between the source and the sink. Using fewer but more sensitive electrodes will also reduce the temporal averaging that is required. The possibility of an electrode being covered by a bubble or bubbles will also be greatly reduced. Since capacitance is proportional to frequency, the electronics will be modified to operate over a 20-50 kHz range to assess this effect. Also, the use of a separate, real-time measurement of liquid conductivity will be investigated as a means of obviating the need for calibration measurements. A code similar to FEMEIT will be written to perform three-dimensional simulations with fairly general conductivity spatial variations.